

# **Shadow Mask Molecular Beam Epitaxy for In-Plane Gradient Permittivity Materials**

Shagorika Mukherjee, Sai Rahul Sitaram, Xi Wang, and Stephanie Law\*

Infrared spectroscopy currently requires the use of bulky, expensive, and/or fragile spectrometers. For gas sensing, environmental monitoring, or other applications, an inexpensive, compact, robust on-chip spectrometer is needed. One way to achieve this is through gradient permittivity materials, in which the material permittivity changes as a function of position in the plane. Here, synthesis of infrared gradient permittivity materials is demonstrated using shadow mask molecular beam epitaxy. The permittivity of the material changes as a function of position in the lateral direction, confining varying wavelengths of infrared light at varying horizontal locations. An electric field enhancement corresponding to wavenumbers ranging from ≈650 to 900 cm<sup>-1</sup> over an in-plane width of  $\approx$ 13  $\mu m$  on the flat mesa of the sample is shown. An electric field enhancement corresponding to wavenumbers ranging from ≈900 to 1250 cm<sup>-1</sup> over an in-plane width of  $\approx$ 13  $\mu$ m on the slope of the sample is also shown. These two different regions of electric field enhancement develop on two opposite sides of the material. This demonstration of a scalable method of creating in-plane gradient permittivity material can be leveraged for the creation of a variety of miniature infrared devices, such as an ultracompact spectrometer.

S. Mukherjee, S. R. Sitaram, X. Wang
Department of Materials Science and Engineering
University of Delaware
201 Dupont Hall, 127 The Green, Newark, DE 19716, USA
S. Law
Department of Materials Science and Engineering
The Pennsylvania State University

University Park, PA 16802, USA E-mail: sal6149@psu.edu S. Law

Materials Research Institute
The Pennsylvania State University
University Park, PA 16802, USA
S. Law

2D Crystal Consortium Materials Innovation Platform The Pennsylvania State University University Park, PA 16802, USA

S. Law

Penn State Institute of Energy and the Environment The Pennsylvania State University University Park, PA 16802, USA

The ORCID identification number(s) for the author(s) of this article can be found under https://doi.org/10.1002/adfm.202411069

© 2024 The Author(s). Advanced Functional Materials published by Wiley-VCH GmbH. This is an open access article under the terms of the Creative Commons Attribution-NonCommercial-NoDerivs License, which permits use and distribution in any medium, provided the original work is properly cited, the use is non-commercial and no modifications or adaptations are made.

DOI: 10.1002/adfm.202411069

### 1. Introduction

Shadow mask molecular beam epitaxy (SMMBE) is a form of selective area epitaxy (SAE) which was developed to enhance the flexibility of conventional molecular beam epitaxy (MBE).[1] As the name suggests, SMMBE uses a mask either directly fabricated on the substrate or placed in contact with the substrate. During film deposition, epitaxial layers are grown<sup>[2]</sup> on the substrate through apertures in the mask. In this way, the film grows only in the desired areas, removing the need for postgrowth etching and the concomitant damage to the film. The use of a mechanical shadow mask for selective MBE growth was first demonstrated by Cho and Reinhart for dielectric waveguide fabrication, with the waveguide width set by the mask dimension.[3,4] Since then, SMMBE has been used for the growth of a wide range of materials and heterostructures.[5-19] Several studies<sup>[1,3,5]</sup> reported a shadowing

effect near the mask edges in which elemental fluxes vary as a function of position. This effect is caused by imperfect mask edges combined with a non-zero angle between the effusion cells and surface normal. This results in a gradient of film thickness and/or composition near the mask edges. The steepness and the width of the gradient can be controlled by varying the mask thickness and/or the angle of the mask edges. In this paper, we demonstrate the potential of the SMMBE technique to create in-plane gradient permittivity materials (GPMs) by taking advantage of the shadowing effect.

A GPM is a material in which the permittivity varies as a function of location. Our aim is to synthesize in-plane GPMs, in which the permittivity varies in the horizontal/in-plane direction rather than in the vertical growth direction. In an in-plane GPM, different wavelengths of light can be confined<sup>[20,21]</sup> at different in-plane locations on the chip. This structure could be used to build an ultracompact on-chip spectrometer. We are interested in working in the infrared (IR) regime, so our GPMs are comprised of heavily silicon-doped indium arsenide (Si:InAs), which is known to be a good IR plasmonic material.<sup>[22–26]</sup> The permittivity of doped semiconductors can be modeled with the Drude formalism as shown in Equation (1):<sup>[27]</sup>

$$\varepsilon_{Drude} = \varepsilon_{\infty} \left( 1 - \frac{\omega_p^2}{\omega^2 + i\omega\Gamma} \right) \tag{1}$$



\_\_\_ FUNCTIONAL \_\_\_ MATERIALS

www.afm-iournal.de

here,  $\varepsilon_{\infty}$  is the high-frequency permittivity of the InAs,  $\omega_p$  is the plasma frequency of the doped InAs,  $\omega$  is the frequency of incident light, and  $\Gamma$  is the electron scattering rate. The plasma frequency,  $\omega_p$ , is related to the carrier density via Equation (2): [28]

$$\omega_p = \sqrt{\frac{ne^2}{\varepsilon_\infty \varepsilon_0 m^* (n)}}$$
 (2)

here, n is the 3D carrier density, e is the carrier charge,  $\varepsilon_{\infty}$  is the high-frequency permittivity of the InAs,  $\varepsilon_0$  is the permittivity of free space, and  $m^*(n)$  is the effective mass of the carriers<sup>[29]</sup> which depends on n.<sup>[28]</sup> InAs can be very heavily doped, with n reaching  $\approx 1 \times 10^{20}$  cm<sup>-3</sup>, which leads to plasma wavelengths as short as  $\approx 5 \, \mu \text{m}$ .<sup>[27]</sup> which is the shortest demonstrated plasma wavelength among the III-V semiconductors. Using MBE to tune the carrier density in Si:InAs enables the plasma wavelength to be tuned across the mid-IR.<sup>[22,27,28]</sup>

Unfortunately, traditional MBE growth can only be used to change the carrier density in the growth direction by changing the silicon and/or the indium fluxes. Creating a GPM using traditional MBE would therefore require the growth of a very thick layer of Si:InAs in which the doping density slowly changes as a function of depth. The sample would then need to be cleaved and the GPM would be fabricated on the cleaved edge. This is technologically challenging, and the resulting devices would be extremely small. Current methods of in-plane GPM fabrication include ion irradiation patterning,<sup>[30]</sup> RF magnetron sputtering,<sup>[31]</sup> and patterned spin-on dopants.<sup>[32]</sup> These techniques have a variety of downsides, such as film damage<sup>[33]</sup> and contamination.<sup>[34]</sup>

To create our GPMs, we use the SMMBE technique. Rather than trying to minimize the flux gradients near the edges of the mask, we aim to enhance and control them. By creating flux gradients of both indium and silicon near the edges of the mask, we can control the permittivity of Si:InAs in the in-plane direction of the film. Each location will thus have a different carrier density, leading to a different plasma frequency,  $\omega_n$ , and ultimately to a different permittivity,  $\varepsilon_{Drude}$ . In this paper, we demonstrate the successful synthesis of a Si:InAs in-plane GPM using SMMBE. We show that we can get in-plane permittivity gradients in our Si:InAs film: on the flat mesa on the side where the silicon flux is shadowed, and on the film slope on the opposite side where the indium flux is shadowed. Using scattering-type scanning nearfield optical microscopy, we see an electric field enhancement for wavenumbers ranging from ≈650 to 900 cm<sup>-1</sup> over an in-plane sample width of ≈13 µm on the flat mesa, and for wavenumbers ranging from ≈900 to 1250 cm<sup>-1</sup> over an in-plane sample width of  $\approx$ 13 µm on the slope. We refer to the wavenumber range as the "spectral gradient" and the in-plane sample width as the "in-plane spatial width." In contrast to the flat mesa, we observe that the inplane permittivity gradient on the slope is steeper and wider and reaches a higher maximum wavenumber of  $\approx 1250$  cm<sup>-1</sup>. Either of the in-plane GPMs on the flat mesa or the slope can be used to build an ultracompact on-chip spectrometer.

#### 2. Results and Discussion

To synthesize our samples, we used removable and potentially reusable shadow masks made of silicon purchased from Norcada (NX10500). Figure 1a shows cross-sectional view of the mask. The mask is 200  $\mu$ m thick and 1  $\times$  1 cm in size with an aperture at the center that is 0.5  $\times$  0.5 cm at the top and 0.528  $\times$  0.528 cm at the bottom with 54.7° sidewalls, shown schematically in Figure 1a. Here the mask is shown in its upsidedown orientation, the way it is inserted into the MBE chamber for sample growth.

The samples comprise a Si:InAs film grown on an unintentionally-doped GaSb (100) single side polished wafer from WaferTech using a Veeco GenXplor MBE system. Each wafer was diced into  $1 \times 1$  cm substrates. During sample growth, the mask was placed on top of the substrate with the larger side of the mask opening in contact with the substrate, as shown in Figure 1b, and the substrate was not rotated. Side 1 of the substrate was fixed toward the silicon dopant cell which placed side 3 closest to the indium cell, enhancing the silicon and indium flux shadowing to obtain the largest in-plane permittivity gradient. The arsenic and bismuth cells were closer to side 4 than side 2, but they were not aligned with a substrate edge. A top-down view of the positions of the cells with respect to the substrate during growth is shown in Figure 1c, displaying the back side of the substrate (brown). Figure 1d shows the front side of the substrate (brown) and the Si:InAs film which is not in the center of the substrate but is offset toward side 1 due to the position of the indium cell. The Si:InAs film has a flat mesa (medium gray) with four mesa edges, as indicated in Figure 1d. Below the mesa edge on each side, the thickness of the Si:InAs varies in the horizontal direction, giving rise to a Si:InAs slope (light gray). The bottom of the Si:InAs slope where the Si:InAs film touches the substrate is the Si:InAs edge, as indicated in Figure 1d. Surrounding the Si:InAs edges, there is a layer of thin deposition on three sides of the sample (dark gray).

The sample is conceptually divided into six regions for ease of discussion, as shown in Figure 1c,d. Regions  $\alpha$ ,  $\beta$ , and  $\delta$  are near side 1, closest to the silicon source. Regions  $\alpha^*$ ,  $\beta^*$ , and  $\delta^*$  are near side 3, closest to the indium source. Regions  $\alpha$  and  $\alpha^*$  are closest to side 2, while regions  $\delta$  and  $\delta^*$  are closest to side 4, near the bismuth and arsenic sources. **Figure 2** shows optical micrographs of the sample taken from regions  $\alpha$ ,  $\alpha^*$ ,  $\delta$ , and  $\delta^*$ . During sample growth, side 4 was closest to the arsenic cell while side 2 was furthest from the arsenic cell; the arsenic beam was therefore shadowed for regions  $\delta$  and  $\delta^*$ . This reduction in arsenic flux impacts the Si:InAs film quality near the mesa edge at side 4, resulting in a dark stripe as shown in Figure 2 (pink arrow).

In addition to the dark stripe, we see thin deposition surrounding the Si:InAs edges. The green dashed boxes in the figure indicate the areas where thin deposition occurs under the overhanging portion of the mask (orange arrow). The widths of these areas vary: side 3 is the widest ( $\approx 300~\mu m$ ), followed by side 4 and side 2. Side 1 has no noticeable deposition. This is because during growth, the indium cell was across from side 1, so there was no shadowing of the indium beam at side 1, resulting in no significant thin deposition and causing the mesa to be offset toward side 1. Side 3 was near the indium cell during growth, so the indium beam was almost fully shadowed for side 3, resulting in the widest area of thin deposition on side 3. The thin depositions occur under the mask overhang: the opening of the mask at the top is 0.5 cm and at the bottom is 0.528 cm, leading





www.afm-journal.de

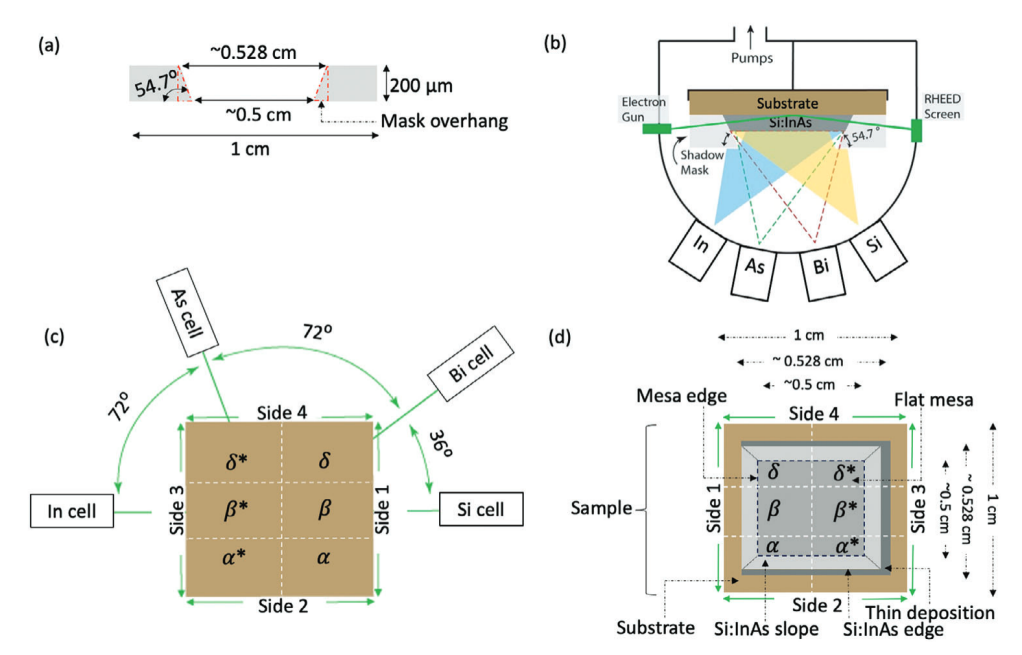


**Figure 1.** a) Cross-sectional view of the silicon shadow mask in its upside-down orientation. b) Sketch of MBE growth chamber showing cross-sectional view of the shadow mask, substrate, and Si:InAs film. c) Top-down view of the positions of the cells with respect to the substrate during sample growth (showing back side of the substrate). d) View of the Si:InAs film (showing front side of the substrate). The sample is divided into six regions:  $\alpha$ ,  $\beta$ ,  $\delta$ ,  $\alpha$ \*,  $\beta$ \* and  $\delta$ \* for ease of discussion. Figures are not to scale.

to mask overhangs which are each 140  $\mu m$  wide on each side of the mask (for details, see Figure 1a and Figure S1, Supporting Information). These mask overhangs give rise to the Si:InAs slopes as well as the thin deposition surrounding the Si:InAs edges. If we consider side 1 and side 3 together, the total mask overhang width is 280  $\mu m$ . This is comparable to the measured thin deposition width of 300  $\mu m$  on side 3. Similarly, thin depositions

occur under the mask overhang on sides 2 and 4, which is caused by partial shadowing of the indium beam since the molecular beam from the cell is not perfectly collimated. The total width of the thin depositions on sides 2 and 4 together is 260  $\mu$ m, which is again comparable to the theoretical width of 280  $\mu$ m. The thin depositions on sides 2 and 4 are not of equal widths due to a slight misalignment of side 3 with respect to the indium cell.

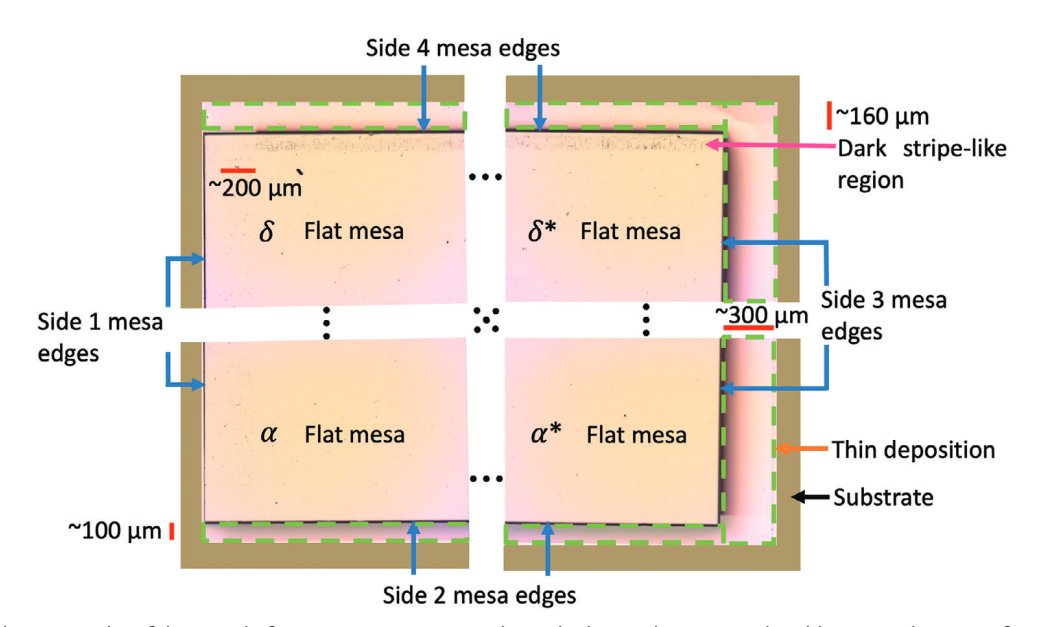


**Figure 2.** Optical micrographs of the sample from regions  $\alpha$ ,  $\alpha^*$ ,  $\delta$ , and  $\delta^*$ . The bare substrate is colored brown in the image for clarity. The brown substrate area remains covered by mask during sample fabrication process. The blue arrows indicate the mesa edges. The dark stripe along the mesa edge of side 4 is indicated by the pink arrow. Thin deposition surrounding the Si:InAs film are indicated by green dashed boxes and labelled by the orange arrow.



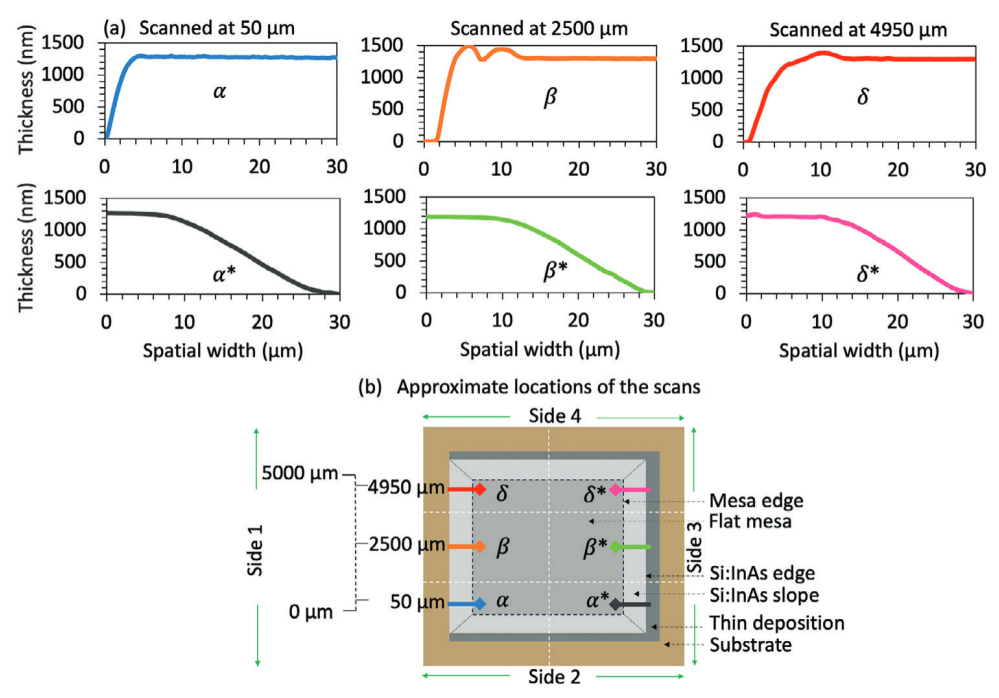


**Figure 3.** a) Surface profiles of the sample from regions  $\alpha$ ,  $\beta$ ,  $\delta$ ,  $\alpha^*$ ,  $\beta^*$ , and  $\delta^*$ . b) Approximate locations and directions of the surface profiles from Figure 3a.

The relative positions of the elemental cells with respect to the substrate during sample growth impact the mesa edges, resulting in variation of the edge profiles, thicknesses, and compositions. Figure 3a shows surface profilometry scans of the sample in the regions  $\alpha$ ,  $\beta$ , and  $\delta$  on side 1 and  $\alpha^*$ ,  $\beta^*$ , and  $\delta^*$  on side 3. The approximate locations of the scans are indicated by the arrows in Figure 3b. We see that the mesa edge on side 1 (closest to silicon; farthest from indium) is not uniform along its length, leading to differences in surface quality. The profiles from regions  $\beta$  and  $\delta$ have large bumps indicative of rougher growth, in contrast to region  $\alpha$  where we see a smoother surface. As described above, during growth, side 4 was closest to the arsenic cell while side 2 was furthest from the arsenic cell. This caused a reduction in arsenic flux for side 4, and an excess of arsenic flux for side 2. As a result, region  $\alpha$  was exposed to an enhanced amount of arsenic in comparison to the neighboring regions  $\beta$  and  $\delta$ , and as such, has a smoother surface. Compared to non-SMMBE growth of Si:InAs, the arsenic flux used for this sample was 1.5× higher to minimize the size of the arsenic-shadowed areas. Region  $\beta$  was directly opposite to the indium source and had maximum exposure to the indium flux, which led to a lower As:In ratio and rougher growth in this region. Chemical analysis of region  $\beta$  (Figure 4b) reveals that the bumps are primarily composed of indium. In contrast to side 1, the mesa edge at side 3 (closest to indium; furthest from silicon) is smoother along its length, as seen in the surface profiles from regions  $\alpha^*$ ,  $\beta^*$ , and  $\delta^*$ . Unlike side 1, side 3 was shadowed from the indium beam during growth. This caused a reduction in the indium flux for side 3, increasing the As:In flux ratio and eliminating the indium droplets. However, region  $\delta^*$ was shadowed from the arsenic flux, lowering the As:In flux ratio compared to the adjacent regions  $\alpha^*$  and  $\beta^*$  and resulting in slightly rougher growth.

We also observe a difference in the Si:InAs mesa slopes on sides 1 and 3: the slope is much steeper on side 1 in comparison to side 3. In particular, the slope on side 1 is  $\approx\!466\pm130~\text{nm}~\mu\text{m}^{-1}$  and on side 3 is  $\approx\!72\pm5~\text{nm}~\mu\text{m}^{-1}$  (see Figure S2, Supporting Information for the linear fits). This is due to the different shadowing of the indium cell. Side 1 was across from the indium cell and therefore had the least shadowing of the indium flux, leading to a steeper slope. Side 3 was closest to the indium cell and therefore experienced the largest shadowing of the indium flux, leading to a shallower slope.

To improve our understanding of the surface morphologies of the sample, SEM images were taken from regions  $\alpha$ ,  $\beta$ , and  $\delta$ , and are shown in Figure 4a. We observe trenches elongated along the [110] direction<sup>[35]</sup> in regions  $\alpha$  and  $\delta$ ; these are marked with black dashed boxes. They appear near the mesa edge of side 2 in region  $\alpha$  and near the mesa edge of side 4 in region  $\delta$ . The trenches correspond to silicon surface segregation as described in references. [35–37] Near the mesa edge of side 1 in regions  $\beta$  and  $\delta$ , sharp-looking structures are marked in white broken boxes. These structures are denser in region  $\delta$  compared to region  $\beta$ , indicating that these features are likely related to the lower As:In flux ratio in this region. Finally, droplet features are observed at the mesa edge of side 1 in region  $\beta$ . Chemical analysis by EDS shown in Figure 4b reveals that these features are primarily composed of indium. Due to the positions of the indium and arsenic sources, region  $\beta$  had the lowest As:In flux ratio, likely resulting in indium droplets. Fortunately, our in-plane permittivity gradient regions are not near the mesa edge of side 1, but much further away; the GPM regions will be discussed later. Figure 4c shows SEM images of regions  $\alpha^*$ ,  $\beta^*$ , and  $\delta^*$ . We again observe trenches elongated along the [110] direction corresponding to silicon surface segregation.[35-37] Due to the positions of the silicon and



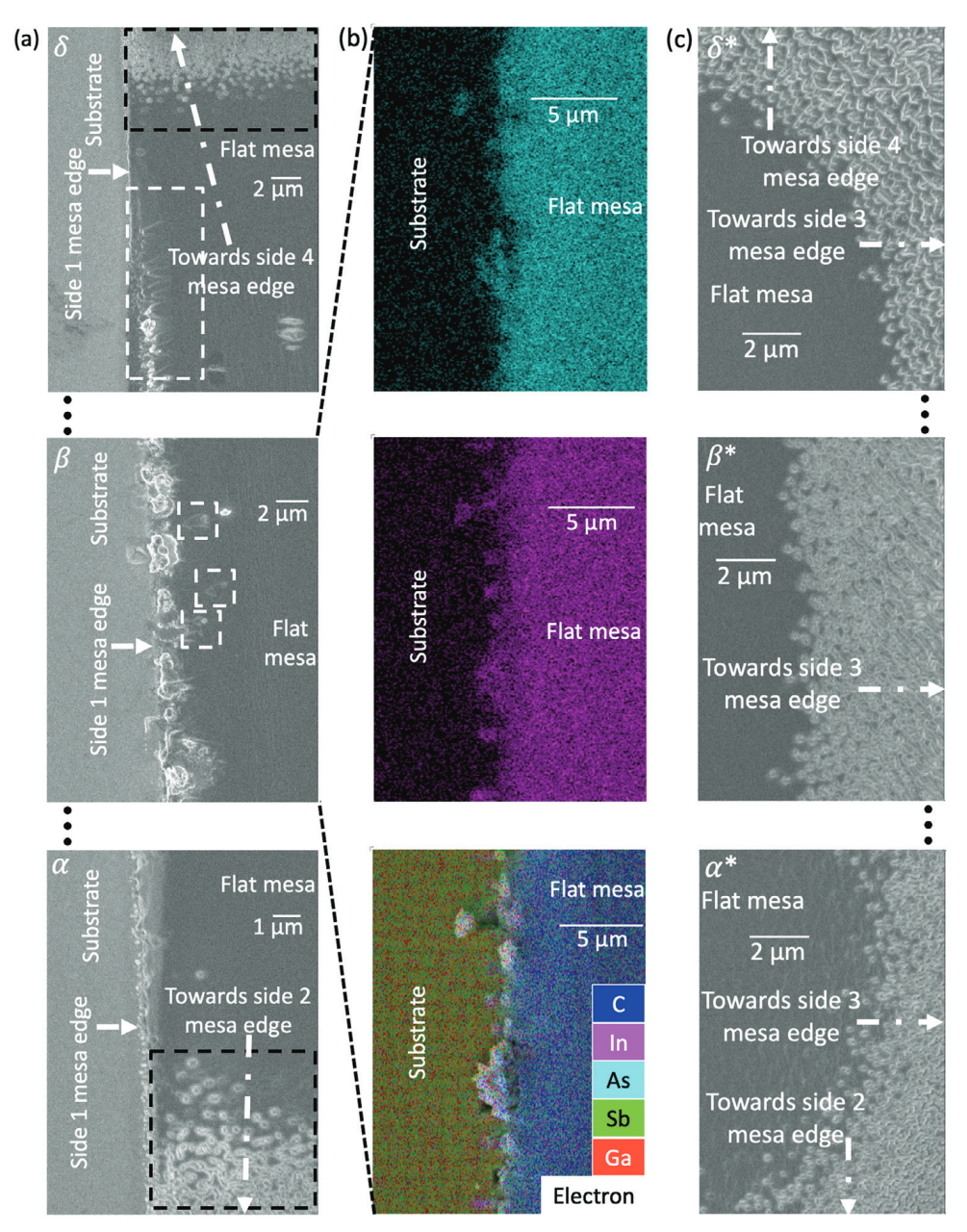


**Figure 4.** a) Surface morphologies via SEM from regions  $\alpha$ ,  $\beta$  and  $\delta$ , respectively. b) Chemical analysis via EDS spectroscopy from region  $\beta$ . c) Surface morphologies via SEM from regions  $\alpha$ \*,  $\beta$ \*, and  $\delta$ \*, respectively. All the images in Figure 4a–c are rotated by 90° in the anti-clockwise direction to match the schematic of our sample orientation.

indium cells, side 3 received a high silicon flux and a low indium flux, leading to excess silicon and promoting silicon surface segregation.

The goal of this project is to create an in-plane silicon doping gradient, giving rise to an in-plane permittivity gradient. We measured the silicon dopant concentration as a function of position using TOF-SIMS; these data are shown in Figure S3 (Supporting Information). To analyze the in-plane permittivity, we used nano-FTIR. Figure 5 shows normalized nano-FTIR spectra as a function of position from regions  $\beta$  and  $\beta^*$ . In both spectra, we see localization and enhancement of different light wavelengths at different positions. The electric field enhancement is calcu-

lated by normalizing the spectra from regions  $\beta$  and  $\beta^*$  of the sample with the spectrum from gold (Au) taken on the same day using the same mid-IR module ( $\approx$ 650–1400 cm<sup>-1</sup>). The normalization was done by dividing the spectra of the respective sample regions by the spectrum of the Au reference. The normalized electric field amplitude is greater than 1, indicating that the electric field is enhanced with respect to the Au reference. For different wavenumbers in the normalized spectra, the enhancement shifts depending on the local permittivity, forming a spectral gradient in both regions  $\beta$  and  $\beta^*$ . The normalized spectra below 650 cm<sup>-1</sup> are noisy because the laser intensity is very low below 650 cm<sup>-1</sup>.



www.afm-journal.de

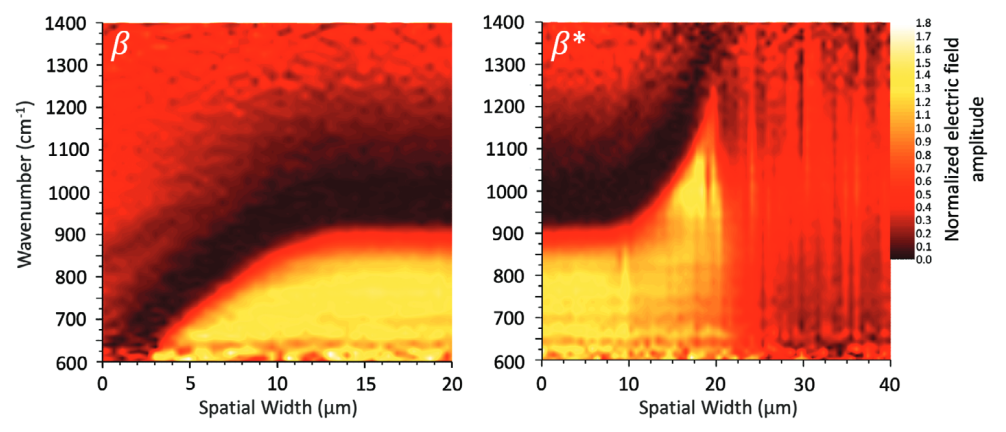
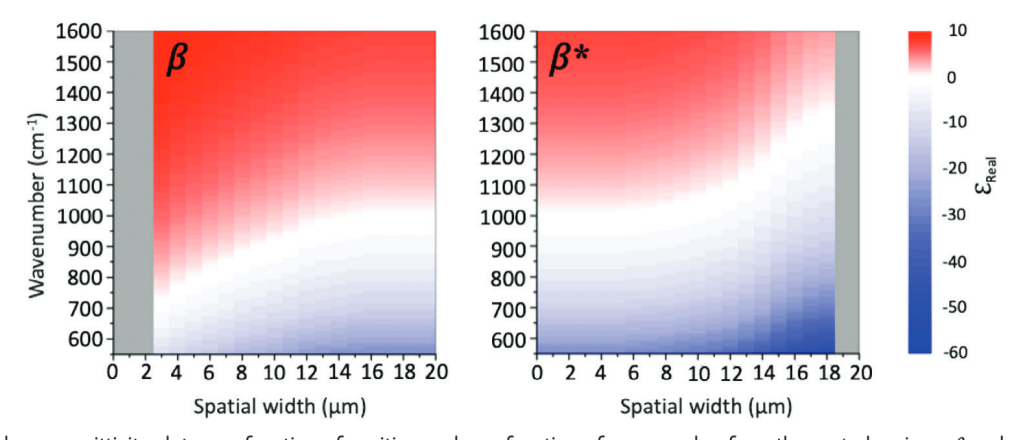


Figure 5. Normalized nano-FTIR spectra from the central regions,  $\beta$  and  $\beta^*$  of the sample with respect to the nano-FTIR spectrum from gold (Au) reference.

To quantify the permittivity gradients from the spectra, we define two parameters: the "spectral gradient width" is the difference between the maximum and minimum wavenumbers in the spectral gradient, and the "spectral gradient steepness" is the ratio of spectral gradient width to the in-plane spatial width. For region  $\beta$ , we see a spectral gradient of 650–900 cm<sup>-1</sup> over an inplane spatial width of 13 µm, giving a spectral gradient width of 250 cm<sup>-1</sup> and a spectral gradient steepness of 19.2 cm<sup>-1</sup>/ $\mu$ m. The spectrum of region  $\beta$  was obtained on the flat mesa at side 1, indicating that the permittivity gradient comes from the variation in silicon flux rather than the variation in indium flux. This matches our expectations, given that this side of the sample had minimal shadowing of the indium flux and maximal shadowing of the silicon flux. Region  $\beta^*$  has a spectral gradient of 900 -1250 cm<sup>-1</sup> over an in-plane spatial width of 13  $\mu$ m, giving a spectral gradient width of 350 cm<sup>-1</sup> and a spectral gradient steepness of 26.9 cm<sup>-1</sup>  $\mu$ m<sup>-1</sup>. Unlike region  $\beta$ , the permittivity gradient in region  $\beta^*$  is not on the flat mesa area; instead, it is on the Si:InAs slope on side 3. Due to the positions of the silicon and indium cells, side 3 received a high silicon flux and a low indium flux. Therefore, the permittivity gradient in this case arises primarily from the variation in indium flux rather than the variation in silicon flux: the silicon flux as a function of position is constant while the indium flux decreases as a function of position in the Si:InAs

slope below the mesa edge. This leads to a concomitant increase in the silicon doping density and gives rise to gradient in permittivity. In contrast to region  $\beta$ , the spectral gradient in region  $\beta^*$  is steeper and wider and reaches a higher maximum wavenumber of  $\approx 1250~\rm cm^{-1}$ . However, after reaching a maximum wavenumber of 1250 cm<sup>-1</sup>, the spectrum becomes extremely noisy. This is likely because the silicon doping density has increased beyond the maximum doping density of InAs, resulting in over-doped areas with poor crystal quality. The non-normalized nano-FTIR spectra for regions  $\alpha$ ,  $\beta$ ,  $\delta$ ,  $\alpha^*$ ,  $\beta^*$  and  $\delta^*$  are given in the Supporting Information in Figures S4 and S5 (Supporting Information). All the spectra in Figures S4 and S5 (Supporting Information) were taken back-to-back on the same day. The respective horizontal and vertical slices of all the non-normalized spectra are shown in Figures S7 and S8 (Supporting Information).

**Figure 6** shows plots of the permittivity of the sample as a function of position and wavenumber from the central regions  $\beta$  and  $\beta^*$  of the sample. The nano-FTIR spectra of regions  $\beta$  and  $\beta^*$  from Figures S4 and S5 (Supporting Information) were used to obtain the approximate plasma frequencies at every 1  $\mu$ m (see Supporting Information for details). The scattering rate corresponding to each plasma frequency was extrapolated from the data in literature.<sup>[38]</sup> Finally, Equation 1 was used to obtain the real part of the permittivity as a function of position and



**Figure 6.** The in-plane permittivity plots as a function of position and as a function of wavenumber from the central regions,  $\beta$  and  $\beta$ \* of the sample.





www.afm-journal.de

Table 1. Step-by-step description of two different mask cleaning methods.

Method 1	Method 2
Sonicate in acetone at room temperature for 1 min	Spray each side of the mask with acetone
Sonicate in isopropanol alcohol (IPA) at room temperature for 1 min	Spray each side of the mask with isopropanol alcohol (IPA)
Blow dry each side of the mask with nitrogen gun	Blow dry each side of the mask with nitrogen gun
Bake each side of the mask on a hot plate at 280 °C	Bake each side of the mask on a hot plate at 280 $^{\circ}$ C

wavenumber. The 2D plots of the permittivity values at every 1  $\mu$ m interval are shown in the Supporting Information in Figures S11 and S12 (Supporting Information). In Figure 6, positive values of the permittivity are shown in red, zero is shown in white, and negative values are shown in blue. We do not have enough data to extract the permittivity for positions 0–2  $\mu$ m in region  $\beta$  or for positions 18–40  $\mu$ m in region  $\beta^*$ , so these regions are covered by gray boxes. From Figure 6, we can see that we have a gradient in permittivity as a function of position and as a function of wavenumber for both regions  $\beta$  and  $\beta^*$ .

#### 3. Conclusions

In conclusion, we have used SMMBE to make in-plane permittivity gradients in Si:InAs thin films. Nano-FTIR spectra as a function of position from our SMMBE Si:InAs film show localization and enhancement of different light wavelengths at different horizontal locations on the film, confirming the formation of in-plane permittivity gradients along the film width. We obtain in-plane permittivity gradients on two opposite sides of the film—on the flat mesa on one side with silicon shadowing and on the film slope on the opposite side with indium shadowing. The permittivity plots as a function of position for a range of wavenumbers further confirm the formation of in-plane permittivity gradients in the SMMBE Si:InAs film. The material quality of the film depends on As:In flux ratio. Regions which had a lower As:In flux ratio showed rougher growth, while regions which had a higher As:In flux ratio showed smoother growth.

Both the in-plane permittivity gradients on the flat mesa and the slope can be used to make devices, such as an on-chip ultracompact spectrometer. However, it is more convenient to work on a flat area in comparison to an area on a slope for device fabrication purposes. In future, the in-plane permittivity gradient width and steepness can be tailored by tailoring the mask design parameters, enabling the design of GPMs tailored to the specific device application.

# 4. Experimental Section

To synthesize the samples, removable and potentially reusable shadow masks made of silicon were used. The first SMMBE trial using as-received mask without cleaning resulted in significant contamination of the sample, leading to institute a cleaning process immediately prior to use. Prior to loading in the MBE chamber, the masks were cleaned with solvents. Two different cleaning methods method 1 and method 2 were used, as described in Table 1. Method 1 worked well, leading to clean masks and no obvious sample contamination. However, over multiple trials, a few masks broke during the cleaning process, likely due to the sonication. As a result, method 2 was tried, which uses the same solvents in the same order, but

without sonication. Method 2 also worked well, leading to clean masks and no obvious sample contamination; no masks broke using method 2.

Prior to film deposition, the substrate was thermally deoxidized under an antimony overpressure. The Si:InAs film was then directly nucleated on top of the substrate at a substrate temperature of 500 °C. A bismuth surfactant was used during the Si:InAs deposition to improve the incorporation of silicon into InAs and to reduce the optical scattering rate.<sup>[35]</sup> The substrate was rotated during deoxidation, but rotation was turned off during Si:InAs deposition to fix side 1 toward the silicon dopant cell. The silicon dopant cell was a filament cell from MBE Komponenten which runs current through a silicon filament to heat the filament and evaporate silicon. This silicon flux was controlled by the filament current, and the temperature of the filament was measured by a non-contact thermocouple. It was found that constant current mode sometimes showed temperature oscillations, and the temperature of the cell dropped by  $\approx 11$  °C over  $\approx 3$  h. The silicon cell current was set at 44 A, and the cell temperature fluctuated between 1032 and 1046 °C. The growth rate was  $\approx 1.89 \ \mu mh^{-1}$ , and the growth time was ≈45 min. The beam equivalent pressure (BEP) of bismuth and arsenic were  $\approx$ 5% indium BEP and  $\approx$ 30× indium BEP, respectively.

After growth, the sample was characterized to determine its physical and optical properties. Optical micrographs were captured with a Zeiss Axio Imager Z2 Vario Microscope. Profilometry scans were used to determine the thickness gradient with a Bruker DektakXT Stylus Profiler. Line scan to measure the intensity of the silicon dopant across the sample was taken with an IONTOF TOF.SIMS<sup>5</sup> time-of-flight secondary ion mass spectrometry (TOF-SIMS). A Neaspec s-SNOM (scattering-type scanning nearfield optical microscope) with a mid-IR module (≈650-1400 cm<sup>-1</sup>) was used to acquire nanoscale Fourier transform infrared (Nano-FTIR) spectra as a function of position to measure the in-plane permittivity gradient using fourth order optical amplitudes along a line on the sample. The Neaspec s-SNOM was also equipped with an AFM unit which was used to acquire  $5 \times 5$  µm area scans for surface roughness values from the approximate locations on the film from where the nano-FTIR spectra were attained. The same AFM unit was used to get the surface profile trends from the approximate locations as the nano-FTIR spectra. Scanning electron microscope (SEM) images were taken to understand the surface morphology of the sample using a Zeiss MERLIN SEM. Energy-dispersive X-ray spectroscopy (EDS) was done to perform chemical analysis on the sample using a Zeiss Auriga 60 SEM tool.

# **Supporting Information**

Supporting Information is available from the Wiley Online Library or from the author.

## **Acknowledgements**

This study was based upon work supported by the U.S. National Science Foundation under award no. ECCS-2102027, the use of facilities and instrumentation supported by the U.S. National Science Foundation through the University of Delaware Materials Research Science and Engineering Center under award no. DMR-2011824, and the use of TOF-SIMS sponsored by the U.S. National Science Foundation, Major Research Instrumentation under award no. DMR-2116754.





www.afm-iournal.de

#### **Conflict of Interest**

The authors declare no conflict of interest.

## **Data Availability Statement**

The data that support the findings of this study are available from the corresponding author upon reasonable request.

## **Keywords**

gradient permittivity materials, infrared, molecular beam epitaxy, plasmonics, semiconductors, shadow masks

> Received: June 24, 2024 Revised: September 5, 2024 Published online:

- T. Schallenberg, Ph.D. Thesis, Bayerischen Julius-Maximilians-Universität 2004.
- [2] G. Kaminsky, J. Vacuum Sci. Technol. B: Microelectron. Nanometer Struct. 1985, 3, 741.
- [3] Y. Luo, L. Zeng, W. Lin, B. Yang, M. C. Tamargo, Y. M. Strzhemechny, S. A. Schwarz, J. Electron. Mater. 2000, 29, 598
- [4] A. Y. Cho, F. K. Reinhart, Appl. Phys. Lett. 1972, 21, 355.
- [5] W. T. Tsang, M. Ilegems, Appl. Phys. Lett. 1977, 31, 301.
- [6] Y. Luo, J. Vacuum Sci. Technol. B: Microelectron. Nanometer Struct. 1998, 16, 1312.
- [7] A. Y. Cho, P. D. Dernier, J. Appl. Phys. 1978, 49, 3328.
- [8] C. Schumacher, W. Faschinger, V. Hock, H. R. Reß, J. Nürnberger, M. Ehinger, J. Cryst. Growth 1999, 201, 599
- [9] K. H. Gulden, X. Wu, J. S. Smith, P. Kiesel, A. Höfler, M. Kneissl, P. Riel, G. H. Döhler, Appl. Phys. Lett. 1993, 62, 3180.
- [10] T. Schallenberg, C. Schumacher, W. Faschinger, Phys. E 2002, 13, 1212
- [11] T. Schallenberg, L. W. Molenkamp, S. Rodt, R. Seguin, D. Bimberg, G. Karczewski, Appl. Phys. Lett. 2004, 84, 963.
- [12] T. Schallenberg, W. Faschinger, G. Karczewski, L. W. Molenkamp, V. Türck, S. Rodt, R. Heitz, D. Bimberg, M. Obert, G. Bacher, A. Forchel, Appl. Phys. Lett. 2003, 83, 446.
- [13] T. Schallenberg, C. Schumacher, K. Brunner, L. W. Molenkamp, Phys. Status Solidi Basic Res. 2004, 241, 564.
- [14] T. Schallenberg, C. Schumacher, L. W. Molenkamp, Phys. Status Solidi (A) Appl. Res. 2003, 195, 232.

- [15] T. Schallenberg, T. Borzenko, G. Schmidt, L. W. Molenkamp, S. Rodt, R. Heitz, D. Bimberg, G. Karczewski, J. Appl. Phys. 2004, 95, 311.
- [16] T. Schallenberg, T. Borzenko, G. Schmidt, M. Obert, G. Bacher, C. Schumacher, G. Karczewski, L. W. Molenkamp, S. Rodt, R. Heitz, D. Bimberg, Appl. Phys. Lett. 2003, 82, 4349.
- [17] T. Schallenberg, K. Brunner, T. Borzenko, L. W. Molenkamp, G. Karczewski, J. Appl. Phys. 2005, 98, 014903
- [18] T. Schallenberg, L. W. Molenkamp, G. Karczewski, Phys. Rev. B Condens. Matter Mater. Phys. 2004, 70.
- [19] N. Tomita, N. Yoshida, S. Shimomura, K. Murase, A. Adachi, S. Hiyamizu, J. Cryst. Growth 1995, 150, 377.
- [20] H. Gao, E. Herrmann, X. Wang, Opt. Express 2020, 28, 1051.
- [21] X. Wang, Y. Deng, Q. Li, Y. Huang, Z. Gong, K. B. Tom, J. Yao, Light Sci. Appl. 2016, 5, e16179.
- [22] S. Law, D. C. Adams, A. M. Taylor, D. Wasserman, *IEEE Photon. Conf.* 2012, 20, 786.
- [23] D. Wei, C. Harris, C. C. Bomberger, J. Zhang, J. Zide, S. Law, Opt. Express 2016, 24, 8735
- [24] J. R. Felts, S. Law, C. M. Roberts, V. Podolskiy, D. M. Wasserman, W. P. King, *Appl. Phys. Lett.* **2013**, 102.
- [25] P. Sohr, D. Wei, S. Tomasulo, M. K. Yakes, S. Law, ACS Photonics 2018, 5.
- [26] P. Sohr, C. I. Ip, S. Law, Opt. Lett. 2019, 44.
- [27] S. Law, L. Yu, D. Wasserman, J. Vacuum Sci. Technol. B. 2013, 31, 03C121.
- [28] S. Law, R. Liu, D. Wasserman, J. Vacuum Sci. Technol. B. 2014, 32, 052601
- [29] D. Wei, C. Harris, S. Law, Opt. Mater. Express 2017, 7, 2672
- [30] A. J. Cleri, M. He, J. D. Caldwell, J. P. Maria, Int. Conf. Metamater., Photonic Crystals Plasmon. 2022, 1205
- [31] H. Dittrich, A. Stadler, D. Topa, H. J. Schimper, A. Basch, Phys. Status Solidi A. 2009, 206, 1034
- [32] A. Rosenberg, J. Surya, R. Liu, W. Streyer, S. Law, L. Suzanne Leslie, R. Bhargava, D. Wasserman, J. Opt. 2014, 16.
- [33] X. Ou, K. H. Heinig, R. Hübner, J. Grenzer, X. Wang, M. Helm, J. Fassbender, S. Facsko, Nanoscale 2015, 7.
- [34] J. Chan, T. Fu, N. W. Cheung, J. Ross, N. Newman, M. Rubin, MRS Proc. 1994, 300, 435.
- [35] D. Wei, S. Maddox, P. Sohr, S. Bank, S. Law, Opt. Mater. Express 2020,
- [36] S. Muto, S. Takeda, M. Hirata, K. Fujii, K. Ibe, *Philos. Mag. A* 1992,
- [37] C. Domke, P. Ebert, M. Heinrich, K. Urban, Phys. Rev. B Condens Matter Mater Phys 1996, 54.
- [38] S. Law, D. C. Adams, A. M. Taylor, D. Wasserman, Opt. Express 2012, 20, 12155.

